DUAL-DOPPLER KINEMATICAL AND DYNAMICAL RETRIEVAL ERRORS IN A SIMULATED SUPERCELL THUNDERSTORM

Corey K. Potvin*[,1], Louis J. Wicker[1], and Alan Shapiro[2]

[1]NOAA/National Severe Storms Laboratory, Norman, OK
[2]School of Meteorology, and Center for the Analysis and Prediction of Storms, University of Oklahoma, Norman, OK

1. INTRODUCTION

Dual-Doppler wind analysis (DDA) is a powerful tool for investigating convective storm structure and processes. However, proper interpretation of DDAs and subsequent dynamical analyses requires thorough understanding of expected errors. Dual- and multiple-Doppler (3+ radars) wind retrieval errors have been systematically examined to varying degrees (e.g., Doviak et al. 1976; Ray et al. 1978; Clark et al. 1980; Kessinger et al. 1987; Given and Ray 1994; Matejka and Bartels 1998). The present study continues this line of investigation, and is concerned with the scenario where two radars are sufficiently close to a supercell thunderstorm to permit motion scales as small as ~ 1 km to be partly resolved (typical of mobile radar datasets).

An observing system simulation experiment (OSSE) framework is adopted whereby DDAs are performed using radar pseudo-observations generated from a numerically-simulated supercell thunderstorm. This allows us to systematically vary the observational characteristics and to precisely evaluate analysis errors. We seek to evaluate errors not just in the DDAs themselves, but also in vorticity, vorticity tendency, parcel trajectory and circulation calculations derived from them. The results are intended to help guide the collection, analysis and interpretation of future mobile radar datasets.

The rest of this paper is organized as follows. Section 2 describes the generation of the numerical supercell simulation and radar pseudo-observations, the DDA technique, the parcel trajectory and circulation calculations, and the analysis verification. Analysis errors and their sensitivity to important radar characteristics are examined in section 3. For brevity, results of experiments exploring the sensitivity of errors to settings in the DDA technique are omitted (these experiments, along with those presented herein, will be described in a future *JTECH* publication). A summary and discussion follow in section 4.

2. METHODS

a. Numerical supercell simulation and radar emulation

The numerical supercell analyzed in our experiments was generated by the National Severe Storms Laboratory Collaborative Model for Multiscale Atmospheric Simulation (NCOMMAS; Wicker and Skamarock 2002; Coniglio et al. 2006). The simulation proceeded on a stationary 102.4 × 102.4 × 20 km domain with 200-m horizontal and vertical spacing. The model was integrated over 2 h using large and small time steps of 2 s and 0.25 s, respectively. A fully dual-moment version of the Ziegler et al. (1985) microphysics scheme (Mansell et al. 2010), referred to herein as the Ziegler Variable Density (ZVD) scheme, was used.

Pseudo-observations of reflectivity Z^{obs} and Doppler velocity V_r^{obs} are generated from the model Z, u, v, and w using a slightly modified version of the Wood et al. (2009) technique to emulate the power-weighted averaging of radial velocities and reflectivities of scatterers within a Gaussian radar beam. To emulate the typical lack of V_r^{obs} in regions of low signal-to-noise ratio, radial velocity observations are only computed in regions with Z^{obs} > 5 dBZ. Random errors (σ = 2 m s^{-1}) are added to the V_r^{obs}.

The scanning characteristics of the emulated radars are representative of storm-scale mobile Doppler radars. The radars sample every 150 m in range and 1.0° in azimuth (except 0.5° in one experiment) and have half-power and effective beam widths of 0.89° and 1.39°, respectively. We use several different volume coverage patterns (VCPs; described later) that represent common scanning strategies used in these deployments. To simulate observational non-simultaneity, the individual sweeps in each VCP are binned by elevation angle, and blocks of sweeps valid at higher elevation angles are computed from model fields valid at later simulation times.

b. Variational dual-Doppler analysis technique

The 3D-VAR DDA technique developed in Shapiro et al. (2009) and Potvin et al. (2012) is used here because of the advantages of the 3D-VAR approach over traditional methods (Gao et al. 1999) and in anticipation of its increased usage by the convective storms community. The technique weakly satisfies the radial wind observations, the anelastic mass conservation equation and a smoothness constraint, and exactly satisfies the impermeability condition at the ground (the vorticity equation constraint tested in the referenced studies was not used in our experiments). The DDAs proceed on a 40 × 40 × 6 km domain with 600 m horizontal and vertical grid spacing. The height of the analysis domain varies with the VCP. To account for translation of the wind field, the V_r^{obs} are backward-advected to the analysis time using constant advection velocity components U and V that are visually estimated from the displacement of Z between two times.

The characteristics of each VCP are listed in Table 1. Using DEEP, the entire depth of the simulated storm

* Corresponding author: Dr. Corey K. Potvin, NOAA/NSSL, National Weather Center, 120 David L Boren Blvd, Norman, OK; email: corey.potvin@noaa.gov.

is sampled by the two radars. SHALLOW permits shorter ΔT (potentially advantageous for parcel trajectory computations) at the expense of not sampling higher altitudes of the storm. OVERSAMP uses the same elevation angles as SHALLOW but has $\Delta\phi$ = 0.5°, thus trading shorter ΔT for increased azimuthal resolution.

c. Vorticity and parcel trajectory retrievals

Vertical vorticity, $\zeta \equiv \partial v/\partial x - \partial u/\partial y$, vertical vorticity tilting, $\dot{\zeta}_{tilt} \equiv -(\partial v/\partial z)(\partial w/\partial x) + (\partial u/\partial z)(\partial w/\partial y)$, vertical vorticity stretching, $\dot{\zeta}_{stre} \equiv -\zeta(\partial u/\partial x + \partial v/\partial y)$ and, in one experiment, horizontal divergence, $\delta \equiv \partial u/\partial x + \partial v/\partial y$ are computed from the dual-Doppler-retrieved winds using centered finite differences valid over 2Δ. In three experiments, the fourth-order Runge-Kutta method is used to backward-compute parcel trajectories from t = 60 min to t = 45 min using the model u, v and w output every 30 s ("true" trajectories) and series of dual-Doppler analyses valid every ΔT + 30 s (analyzed trajectories)[1]. In both cases, the trajectory time step is 1 s. In addition, circulation, $\Gamma \equiv \sum_C \boldsymbol{V} \bullet d\boldsymbol{l}$, where $\boldsymbol{V}$ is the mean wind vector along a line segment position vector $d\boldsymbol{l}$, is computed around material circuits C connecting the parcel trajectories at successive times.

d. Verification

The verification wind fields are generated from the simulated fields using two steps. First, to match the motion scales in the analyses that can be resolved on the analysis grid, a sixth-order implicit filter (Raymond 1988) is used to strongly damp wavelengths < 1.2 km (2Δ) in the 200-m simulated wind fields. Second, to verify the retrievals on the analysis grid points, the verification winds are computed at each analysis point by taking a weighted average of all the filtered verification winds located on and within the a (600 m)^3 grid box centered on each analysis point. The verification winds valid on surfaces and edges of the (600 m)^3 grid box are weighted ½ and ¼ as much, respectively, as winds valid within the 600-m grid box. The verification ζ, $\dot{\zeta}_{tilt}$ and $\dot{\zeta}_{stre}$ are computed from the verification u, v and w using the same finite differencing stencil as in the analysis procedure.

Verification is performed only within the dual-Doppler domain, defined in this study as the set of analysis points located within 750 m of at least one V_r^{obs} from each radar. All statistics presented herein are computed within horizontal planes of the dual-Doppler domain. To facilitate the interpretation of the RMS error (RMSE) and relative RMSE (RRMSE; RMSE as a percentage of the RMS truth) plots presented below, vertical RMS profiles of the verification (hereafter, "true") variables are shown in Fig. 1.

[1] We performed dual-Doppler analyses every ΔT + 30 s rather than every ΔT to account for the time required for the radar dish to return to its base tilt.

3. RESULTS

a. Control experiment

A DDA (hereafter labeled CTRL) was performed using observations collected by two radars having the sampling characteristics listed in section 2a and using the DEEP VCP (Table 1). The radars were positioned to produce a 60° cross-beam angle (CBA) at the domain center, which is roughly collocated with the storm's hook echo reflectivity signature at 60 min into the simulation (Fig. 2), the time at which all retrievals in this study are valid. Prior to CTRL, a series of preliminary dual-Doppler retrievals was performed in which the method for interpolating between the observational and analysis grids and the values of the constraint weights used in the 3D-VAR procedure were varied. The settings that produced the "best" analysis (that which recovered as much of the amplitude of local extrema in the kinematical fields as possible while maintaining acceptably low noise levels) were adopted in CTRL and as the default settings in the remaining retrieval experiments. The analysis errors that occurred in CTRL are shown in Fig. 3.

The RMSE and RRMSE in all six analyzed variables generally increase with height, especially at upper levels of the analysis domain, with the RMSE in all three wind components exceeding 10 m s^{-1} near the domain top. The degradation of the analysis with height is partly attributable to the increasing vertical distance between successive radar scans. The RRMSE in w^a exceeds 40 % at all levels above the surface. As expected, smaller relative errors occur in u^a and v^a, however, u^a errors exceed 30 % even at some lower levels, and v^a errors approach those in w^a at higher levels. Due to spatial discretization errors, relative errors in ζ^a are substantially larger than those in u^a and v^a, and relative errors in δ^a, $\dot{\zeta}_{tilt}$ and $\dot{\zeta}_{stre}$ generally far exceed those in all three wind components. The degradation of the retrieved fields between z = 0.6 km and the surface indicates the 3DVAR framework does not substantially mitigate errors arising from lacking radar data near the ground.

Vertical correlation profiles (fig. 3d) as well as comparisons of horizontal cross-sections of the true and analyzed variables (shown for selected variables and heights in Fig. 4) reveal that much of the RMSE increase with height arises from increasing mismatch between the true and retrieved wind field patterns. Much of this mismatch at higher levels (see Fig. 4e,f) is due to the retrieved wind field being displaced to the east of the true wind field, indicating that our (constant) estimate for U (= 10 m s^{-1}) is too small aloft. This motivated a new set of experiments in which U was alternately increased to 12.5, 15.0, 17.5 and 20.0 m s^{-1} (but still held constant over the analysis domain). None of the resulting analyses (not shown) were substantially better than the CTRL analysis, indicating that our use of spatially-

constant advection correction was too simple for this case. Visual inspection of the model wind fields at successive times (not shown) suggests much of the error at higher levels also results from substantial intrinsic (i.e., Lagrangian) evolution of the flow (for which no provision is made in the retrieval technique) between the analysis time and the times at which upper-level observations are valid.

These results suggest that the analysis errors, especially at higher levels, might have been substantially reduced had more sophisticated methods been used to account for flow advection and intrinsic evolution. Since our primary objective is to examine typical errors in storm-scale 3D-VAR dual-Doppler wind syntheses, we did not attempt to use more specialized methods to correct for these processes (e.g., Shapiro et al. 2010a,b; Potvin et al. 2012). The errors arising from unaccounted wind field advection and evolution in our case is examined in section 3c. From the results already presented we conclude that, given a typical storm-topping mobile radar scanning strategy and method of correcting for flow advection and evolution, caution should be exercised when interpreting 3D-VAR dual-Doppler analyses at high altitudes.

b. Impact of cross-beam angle

Owing to the many difficulties inherent to mobile radar storm intercepts (e.g., radar siting, road network limitations, rapid and/or variable storm motion), CBAs are often very suboptimal (i.e., much less than 90°). To explore the sensitivity of the analyses to the CBA, CTRL was performed with Rad2 successively repositioned to effect CBAs at the analysis domain center of ~90° or ~30° (CBA90 and CBA30, respectively). The distances of the radars to the center of the domain remained the same as in CTRL. The relocated Rad2 positions are shown in Fig. 2.

Increasing the CBA from 60° to 90° did not substantially improve the analysis (Fig. 5). Decreasing the CBA from 60° to 30° had a larger (detrimental) impact on the RMSE, but the CBA30 fields were still reasonably accurate (Figs. 5, 6). These results are encouraging given the difficulty of realizing large CBAs in mobile radar deployments. The impact of small CBAs on parcel trajectory calculations is examined in Section 3d.

c. Impact of scanning strategy

One common alternative to using a deep-scanning strategy is to sample only the lower/middle levels of the storm. This reduces ΔT and, thus, the interval between successive dual-Doppler analyses (the impact of shorter ΔT on parcel trajectory calculations is examined in Section 3d). To explore the impact of omitting upper-level radar observations on the analysis, we performed a retrieval experiment using the SHALLOW VCP (Table 1; Fig. 7). Fortunately, excluding upper-level observations did not substantially degrade the analysis at lower levels. Repeating the SHALLOW retrieval with an azimuthal increment of 0.5° and thus twice as large a ΔT (i.e., OVERSAMP) increased the RMSE at all levels. Some kinematical features were better resolved using the OVERSAMP VCP due to the enhanced spatial resolution (not shown). However, errors from flow unsteadiness grew due to the longer periods between the analysis and observation times relative to the retrievals with DEEP and SHALLOW, resulting in a net RMSE increase. This result highlights the importance of considering the tradeoffs between spatial resolution and volume scan time when designing scanning strategies.

To examine the impact of wind field unsteadiness errors on our analyses, CTRL was repeated using an instantaneous version (ΔT = 0) of DEEP (INSTANT). The resulting error reduction, particularly at higher analysis levels, was very large (Fig. 7). Evidently, the limited ability of our simple advection-correction method to account for the complex evolution of the wind field between the analysis and observation times, particularly at higher levels, was a major source of errors in our analyses. It is possible that these errors could be substantially reduced through a more sophisticated advection-correction method (e.g., the spatially-variable technique of Shapiro et al. 2010a,b). Even in that case, however, accounting for the intrinsic flow evolution would remain very challenging (e.g., Potvin et al. 2012). Thus, using rapidly scanning radars may be the more effective strategy for reducing errors due to wind field unsteadiness. In the absence of rapid-scan data, it is strongly recommended that dual-Doppler retrievals of upper-level winds in supercells use advanced methods to account for flow unsteadiness.

d. Parcel trajectory and circulation analyses

To explore the potential impacts of some of the retrieval errors examined above on interpretation of supercell dynamics, 1000 parcel trajectories were initiated around a 3-km-radius ring centered between the main updraft and downdraft at z = 1.2 km using the model winds and the CTRL (section 3a), CBA30 (section 3b) and SHALLOW (section 3c) wind analyses. Horizontal and x-z projections of the material circuits connecting the trajectories at t = 57 min and t = 50 min (3 and 10 minutes prior to the dual-Doppler analysis time, respectively) in each case are shown in Figs. 8a and 8b. Encouragingly, all three dual-Doppler analyses permitted qualitatively accurate diagnoses of the source regions of air in the potentially tornadic region of the storm. The timing of the rapid increase of circulation experienced by the circuit after t = 55 min was also well-retrieved in all three experiments (Fig. 8c). However, the substantial underestimation of circulation at earlier times, and consequent overestimation of the increase in circulation prior to t = 55 min, would imply (via the Bjerknes circulation theorem) much larger baroclinic contribution to circulation (~7×10^5 m^2 s^{-1}) than actually occurred during this period (~5×10^5 m^2 s^{-1}).

The smaller ΔT in SHALLOW enabled more accurate retrieval of parcel trajectories in regions of strongly curved flow, and improved the circulation

analysis after $t \approx 57$ min. These results suggest that shallower scanning strategies will benefit investigations of low-level supercell dynamics. Fortunately, the parcel trajectory errors were only moderately larger in CBA30 than in CTRL, and the circulation analysis was roughly as good in both cases. This suggests quasi-optimal CBAs are not required for useful dynamical information to be inferred from low-level supercell wind analyses.

4. SUMMARY AND DISCUSSION

Given the ubiquity and scientific value of dual-Doppler wind retrievals in studies of supercell thunderstorms, improved knowledge of the errors characteristic of these and subsequent, dynamical retrievals should facilitate progress in understanding supercell behavior. The OSSE framework adopted for this study permitted precise evaluation of these errors and their sensitivity to a number of recognized dual-Doppler retrieval error sources. We chose to emulate close-range mobile radar datasets in our experiments since they are increasingly common and, owing to their relatively high spatiotemporal resolution, have enhanced potential to illuminate supercell kinematics and dynamics.

Many of the results were encouraging with regard to analysis errors. Similar wind and vorticity analyses were obtained using two of the most popular interpolation methods (Barnes or Cressman), and the results were not unduly sensitive to the specification of the shape parameter or influence radius (results omitted for brevity). Additionally, the analyses were not very sensitive to errors in the estimated hydrometeor fall speeds (not shown), nor to the omission of upper-level radar observations. The latter result suggests that confining volume coverage patterns to the region of interest may be a viable strategy for reducing volume scan times. Finally, low-level parcel trajectories initiated near the main updraft and RFD were qualitatively accurate, as were time series of circulation along the computed material circuits.

On the other hand, significant errors arose from several sources in the analyses. The magnitudes of local extrema in the retrieved vorticity and vorticity tendency fields were sensitive to the relative weight of the smoothness constraint in the analysis (not shown). This problem is not unique to the 3D-VAR approach; spatial filtering is also required in traditional dual-Doppler retrievals when high-amplitude noise would otherwise arise in the analysis. The assumptions of spatially constant storm motion and zero storm-relative flow evolution led to significant errors in the analyzed wind field position and pattern at middle and upper levels. In addition, improved spatial resolution of the wind fields due to azimuthal oversampling were countered by increased flow unsteadiness errors due to longer periods between the analysis and observation times. These results highlight the importance of considering the tradeoff between spatial and temporal resolution when designing scanning strategies. To the extent that the translation and evolution of real supercell wind fields is as rapid and complex as that in our simulation, it would likely be very difficult to accurately account for flow unsteadiness in the dual-Doppler analyses.

The locally large errors in the retrieved horizontal divergence, vorticity and vorticity tendency fields and in the circulation analyses imply that *hypotheses relying heavily upon the quantitative accuracy of such variables should be viewed with caution*. This is especially true very near the ground, where lack of Doppler velocity observations can result in severe analysis errors even in the 3D-VAR framework. On the other hand, the results also suggest that inferences about supercell behavior based on qualitative features in 3D-VAR storm-scale dual-Doppler wind syntheses and subsequent dynamical retrievals may generally be reliable.

Acknowledgments. The first author was supported by a National Research Council Postdoctoral Award at the NOAA National Severe Storms Laboratory.

References

Clark, T. L., F. I. Harris, and C. G. Mohr, 1980: Errors in wind fields derived from multiple-Doppler radars: Random errors and temporal errors associated with advection and evolution. *J. Appl. Meteor.*, **19**, 1273–1284.

Coniglio, M. C., D. J. Stensrud, and L. J. Wicker, 2006: Effects of upper-level shear on the structure and maintenance of strong quasi-linear mesoscale convective systems. *J. Atmos. Sci.*, **63**, 1231–1252.

Doviak, R. J., P. S. Ray, R. G. Strauch, and L. J. Miller, 1976: Error estimation in wind fields derived from dual-Doppler radar measurement. *J. Appl. Meteor.*, **15**, 868–878.

Gao, J., M. Xue, A. Shapiro, and K. K. Droegemeier, 1999: A variational method for the analysis of three-dimensional wind fields from two Doppler radars. *Mon. Wea. Rev.*, **127**, 2128–2142.

Given, T., and P. S. Ray, 1994: Response of a two-dimensional dual-Doppler radar wind synthesis. *J. Atmos. Oceanic Technol.*, **11**, 239–255.

Kessinger, C. J., P. S. Ray, and C. E. Hane, 1987: The Oklahoma squall line of 19 May 1977. Part I: A multiple Doppler analysis of convective and stratiform structure. *J. Atmos. Sci.*, **44**, 2840–2865.

Mansell, E. R., C. L. Ziegler, and E. C. Bruning, 2010: Simulated electrification of a small thunderstorm with two-moment bulk microphysics. *J. Atmos. Sci.*, **67**, 171–194.

Matejka, T., and D. L. Bartels, 1998: The accuracy of vertical air velocities from Doppler radar data. *Mon. Wea. Rev.*, **126**, 92–117.

Potvin, C. K., A. Shapiro, and M. Xue, 2012: Impact of a vertical vorticity constraint in variational dual-Doppler wind analysis: Tests with real and simulated supercell data. *J. Atmos. Oceanic Technol.*, **29**, 32-49.

Ray, P. S., K. K. Wagner, K. W. Johnson, J. J. Stephens, W. C. Bumgarner, and E. A. Mueller, 1978: Triple-Doppler observations of a convective storm. *J. Appl. Meteor.*, **17**, 1201–1212.

Raymond, W. H., 1988: High-order low-pass implicit tangent filters for use in finite area calculations. *Mon. Wea. Rev.*, **116**, 2132–2141.

Shapiro, A., C. K. Potvin, and J. Gao, 2009: Use of a vertical vorticity equation in variational dual-Doppler wind analysis. *J. Atmos. Oceanic Technol.*, **26**, 2089–2106.

——, K. M. Willingham, and C. K. Potvin, 2010: Spatially variable advection correction of radar data. Part I: Theoretical considerations. *J. Atmos. Sci*, **67**, 3445-3456.

——, ——, and ——, 2010: Spatially variable advection correction of radar data. Part II: Test results. *J. Atmos. Sci*, **67**, 3457-3470.

Wicker, L. J., and W. C. Skamarock, 2002: Time-splitting methods for elastic models using forward time schemes. *Mon. Wea. Rev.*, **130**, 2088–2097.

Wood, V. T., R. A. Brown, and D. C. Dowell, 2009: Simulated WSR-88D velocity and reflectivity signatures of numerically modeled tornadoes. *J. Atmos. Oceanic Technol.*, **26**, 876–893.

Ziegler, C. L., 1985: Retrieval of thermal and microphysical variables in observed convective storms. Part 1: Model development and preliminary testing. *J. Atmos. Sci.*, **42**, 1487–1509.

	ΔT (min)	Z_{TOP} (km)	$\Delta\phi$ (°)	Elevation angles θ (°)
DEEP	2.5	13.8	1.0	0.5, 1.5, 2.5, 3.5, 4.5, 6.0, 7.5, 9.0, 10.5, 12.5, 14.5, 16.5, 19.0, 21.5, 24.0, 27.0, 30.0, 33.0
INSTANT	0.0	13.8	1.0	0.5, 1.5, 2.5, 3.5, 4.5, 6.0, 7.5, 9.0, 10.5, 12.5, 14.5, 16.5, 19.0, 21.5, 24.0, 27.0, 30.0, 33.0
SHALLOW	1.5	6.0	1.0	0.5, 1.5, 2.5, 3.5, 4.5, 6.0, 7.5, 9.0, 10.5, 12.5, 14.5, 16.5
OVERSAMP	3.0	6.0	0.5	0.5, 1.5, 2.5, 3.5, 4.5, 6.0, 7.5, 9.0, 10.5, 12.5, 14.5, 16.5

Table 1. Volume coverage patterns used in retrievals.

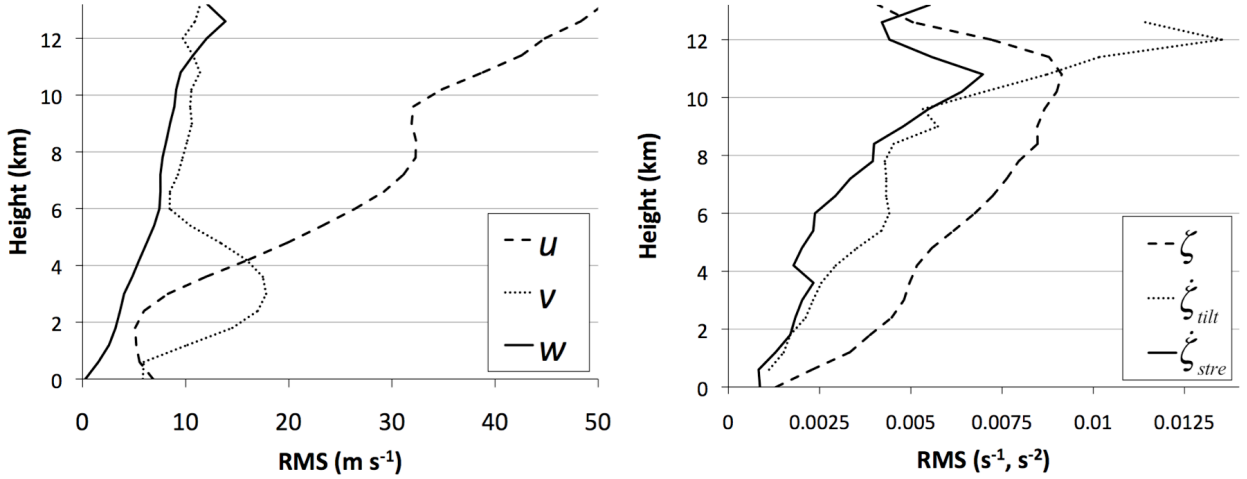

Fig. 1. Vertical RMS profiles of true fields: (left) u (m s^{-1}; dashed), v (m s^{-1}; dotted) and w (m s^{-1}; solid); (right) ζ (s^{-1}; dashed), $\dot{\zeta}_{tilt}$ (× 100 s^{-2}; dotted) and $\dot{\zeta}_{stre}$ (× 100 s^{-2}; solid).

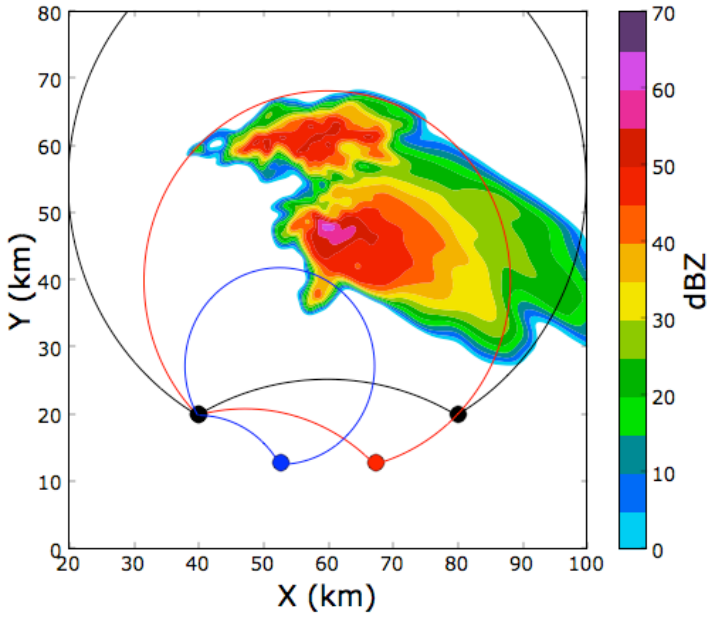

Fig. 2. True Z (shading) and Rad2 locations (dots) for retrievals with CBA=90° (black), CBA = 60° (red) and CBA = 30° (blue) near analysis domain center. The northern 30° dual-Doppler lobe is depicted in each case. The dual-Doppler analysis domain is outlined by the black, dashed square.

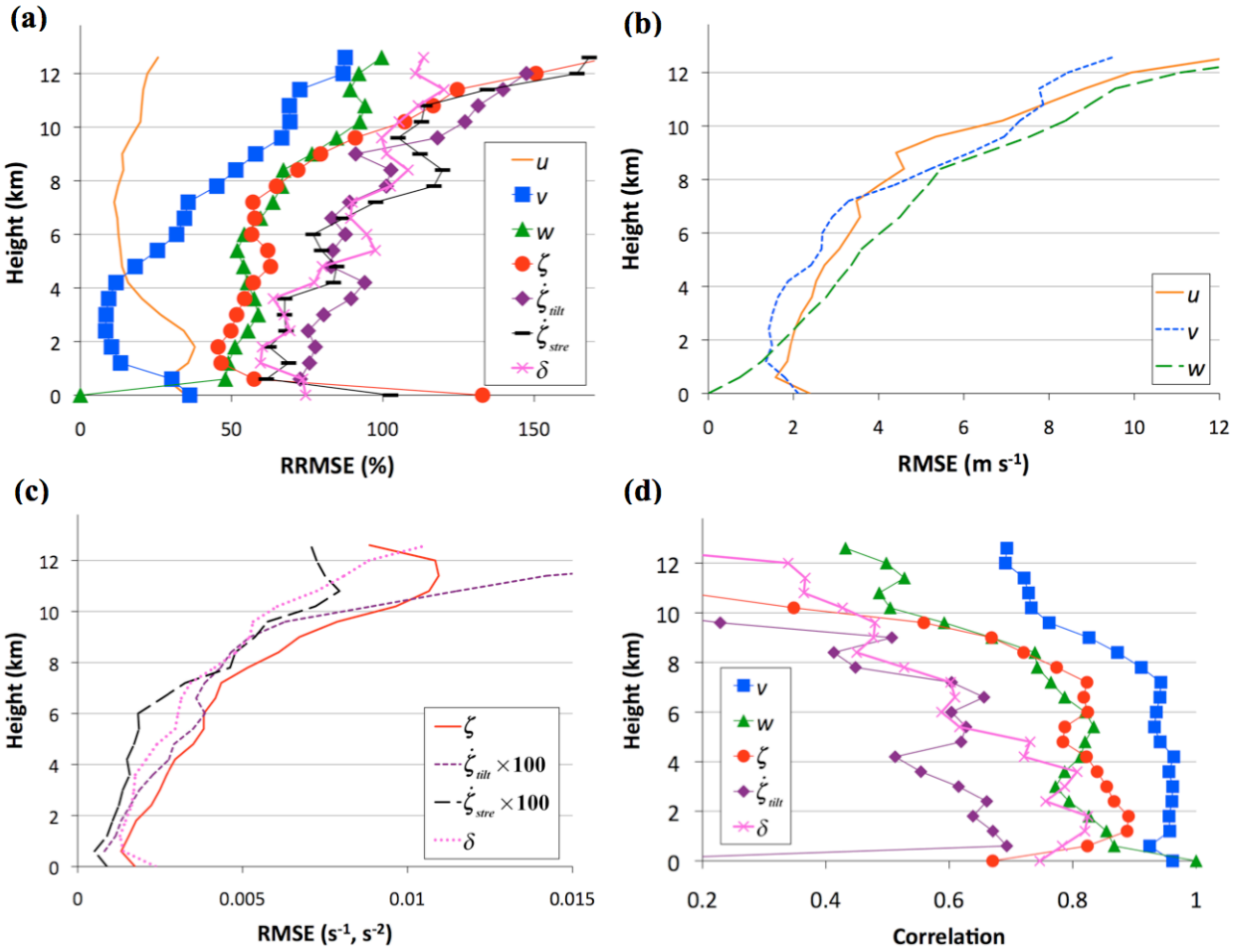

Fig. 3. Errors in CTRL: (a) RRMSE (%) u^a (plain), v^a (squares), w^a (triangles), ζ^a (circles), $\dot{\zeta}^a_{tilt}$ (diamonds), $\dot{\zeta}^a_{stre}$ (bars), and δ^a (crosses); (b) RMSE u^a (solid), v^a (short-dashed) and w^a (long-dashed); (c) RMSE ζ^a (solid), RMSE δ^a (dotted), 100 × RMSE $\dot{\zeta}^a_{tilt}$ (short-dashed) and 100 × RMSE $\dot{\zeta}^a_{stre}$ (long-dashed); (d) correlations of true fields with v^a (squares), w^a (triangles), δ^a (crosses), ζ^a (circles), and $\dot{\zeta}^a_{tilt}$ (diamonds).

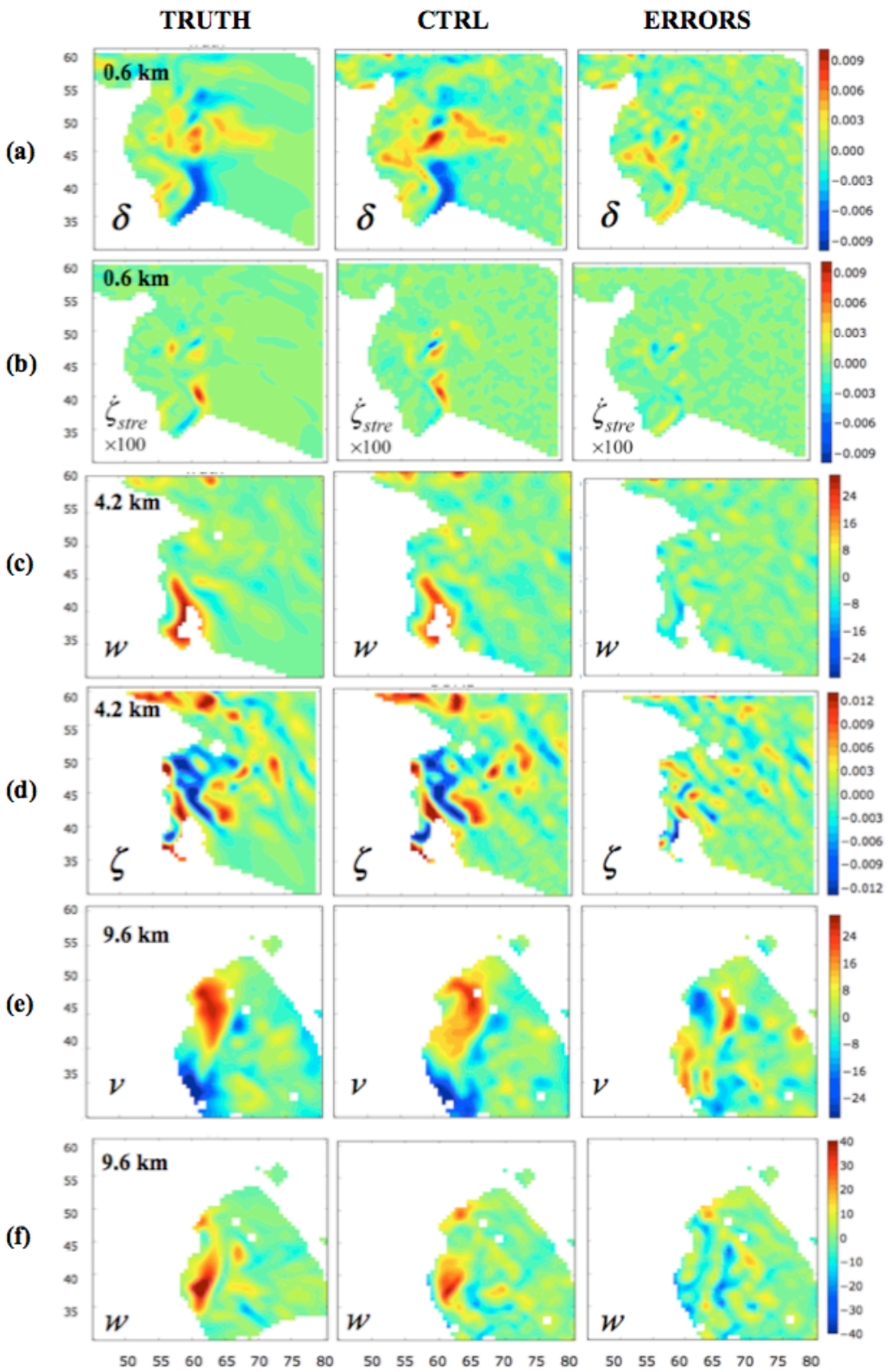

Fig. 4. Horizontal cross-sections of (left column) true, (middle column) analyzed, and (right column) analysis errors in (a) δ at z = 0.6 km, (b) 100 × $\dot{\zeta}_{stre}$ at z = 0.6 km, (c) w at z = 4.2 km, (d) ζ at z = 4.2 km, (e) v at z = 9.6 km, and (f) w at z = 9.6 km. Variables in this and subsequent figures are only plotted where observations from both radars are available within 750 m of the analysis point.

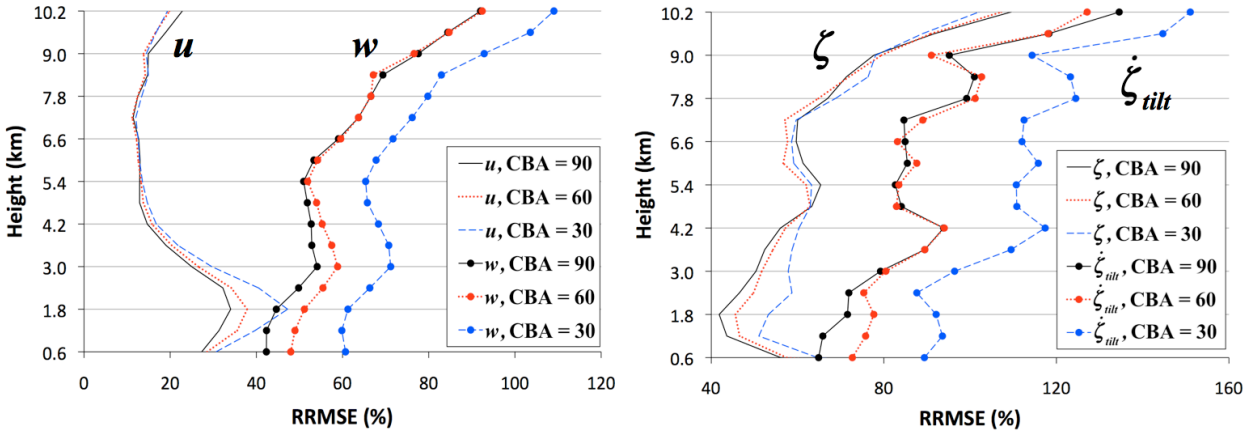

Fig. 5. RRMSE (%) for retrievals with CBA = 90° (CTRL; solid) and Rad2 relocated to produce CBA = 60° (short-dashed) and CBA = 30° (long-dashed): (left) u^a (plain) and w^a (circles); (right) ζ^a (plain), $\dot{\zeta}^a_{tilt}$ (circles).

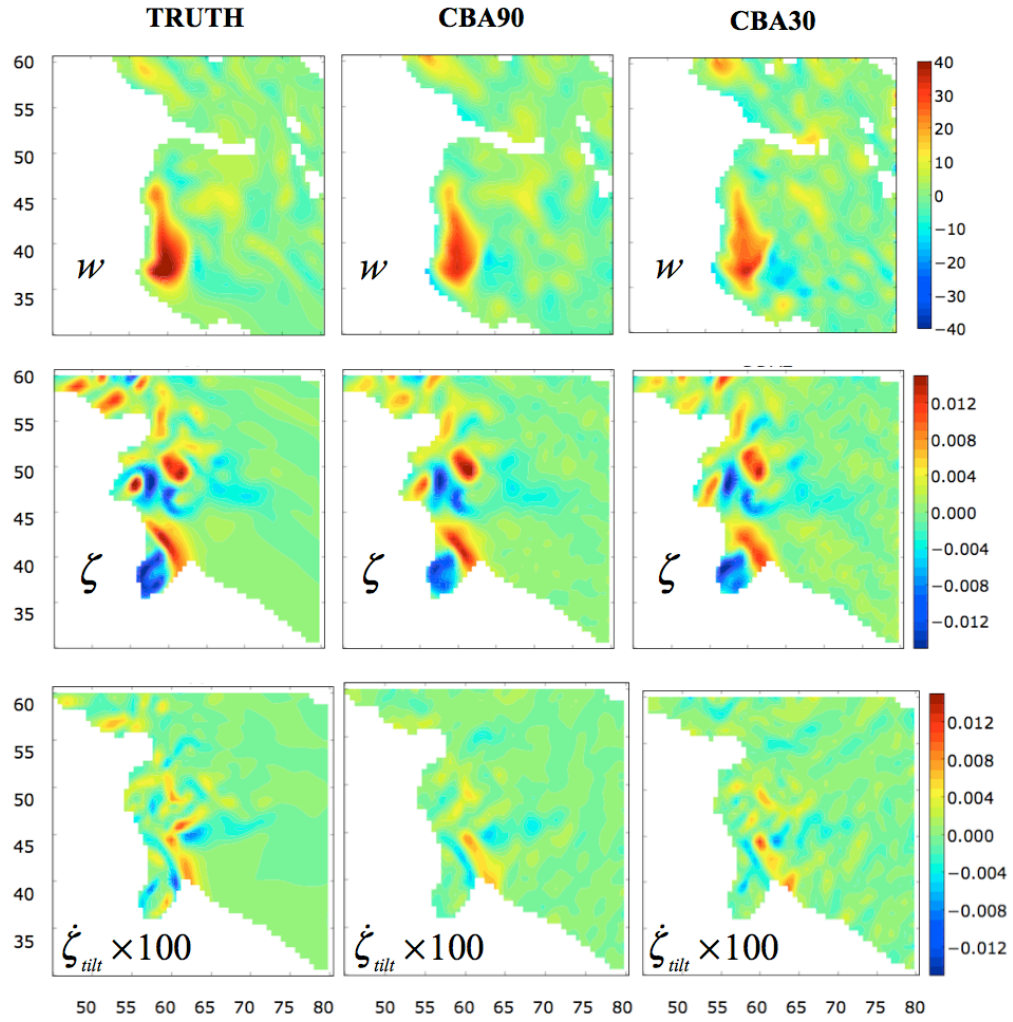

Fig. 6. Horizontal cross-sections of (left column) true fields and fields retrieved using (middle column) CBA = 90° and (right column) CBA = 30°: (top row) w at z = 6.0 km; (middle row) ζ at z = 1.8 km; (bottom row) $\dot{\zeta}_{tilt} \times 100$ at z = 1.8 km.

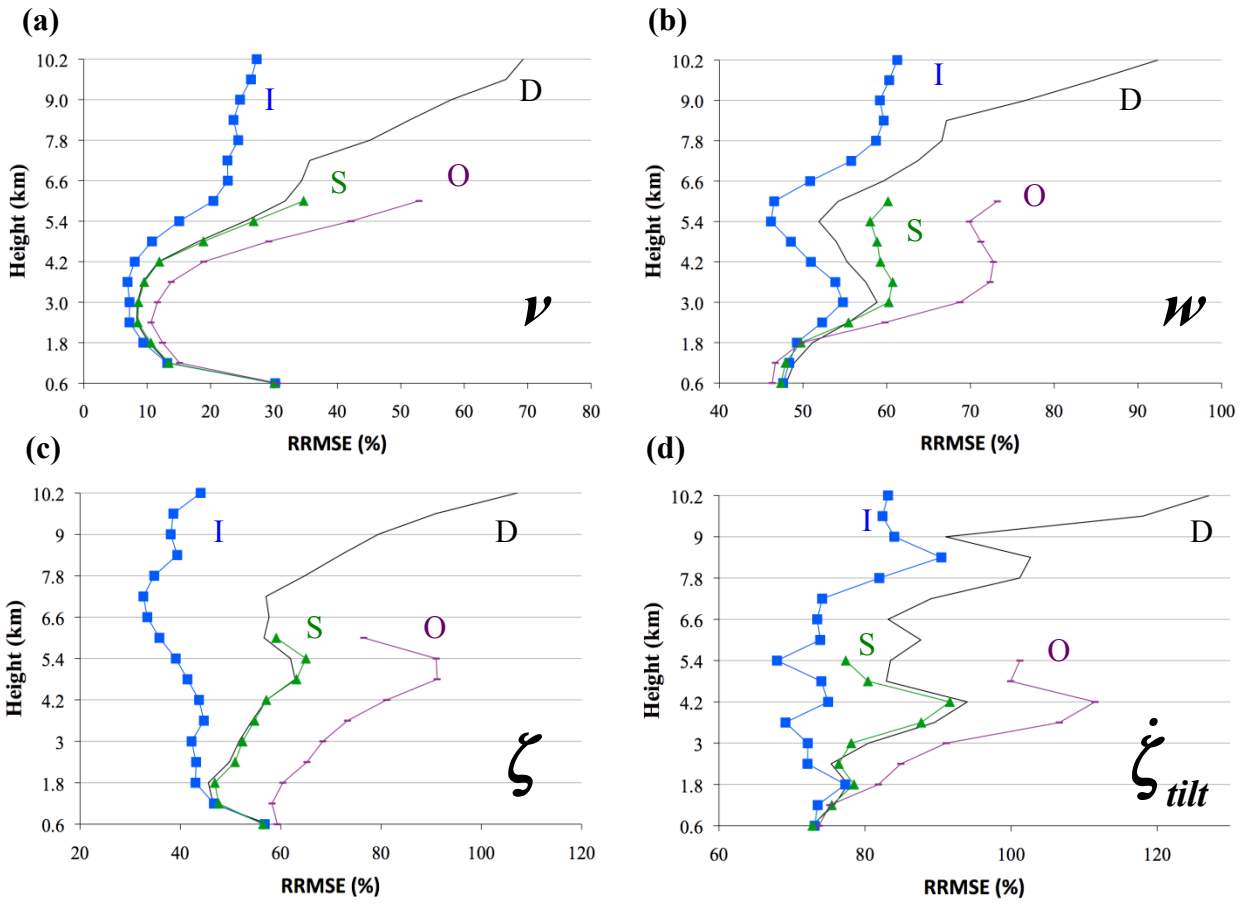

Fig. 7. RRMSE (%) for DEEP (plain), SHALLOW (triangles), OVERSAMP (violet), and INSTANT (squares): (a) v^a, (b) w^a, (c) ζ^a, (d) $\dot{\zeta}^a_{tilt}$. Initials next to the curves represent their corresponding VCPs.

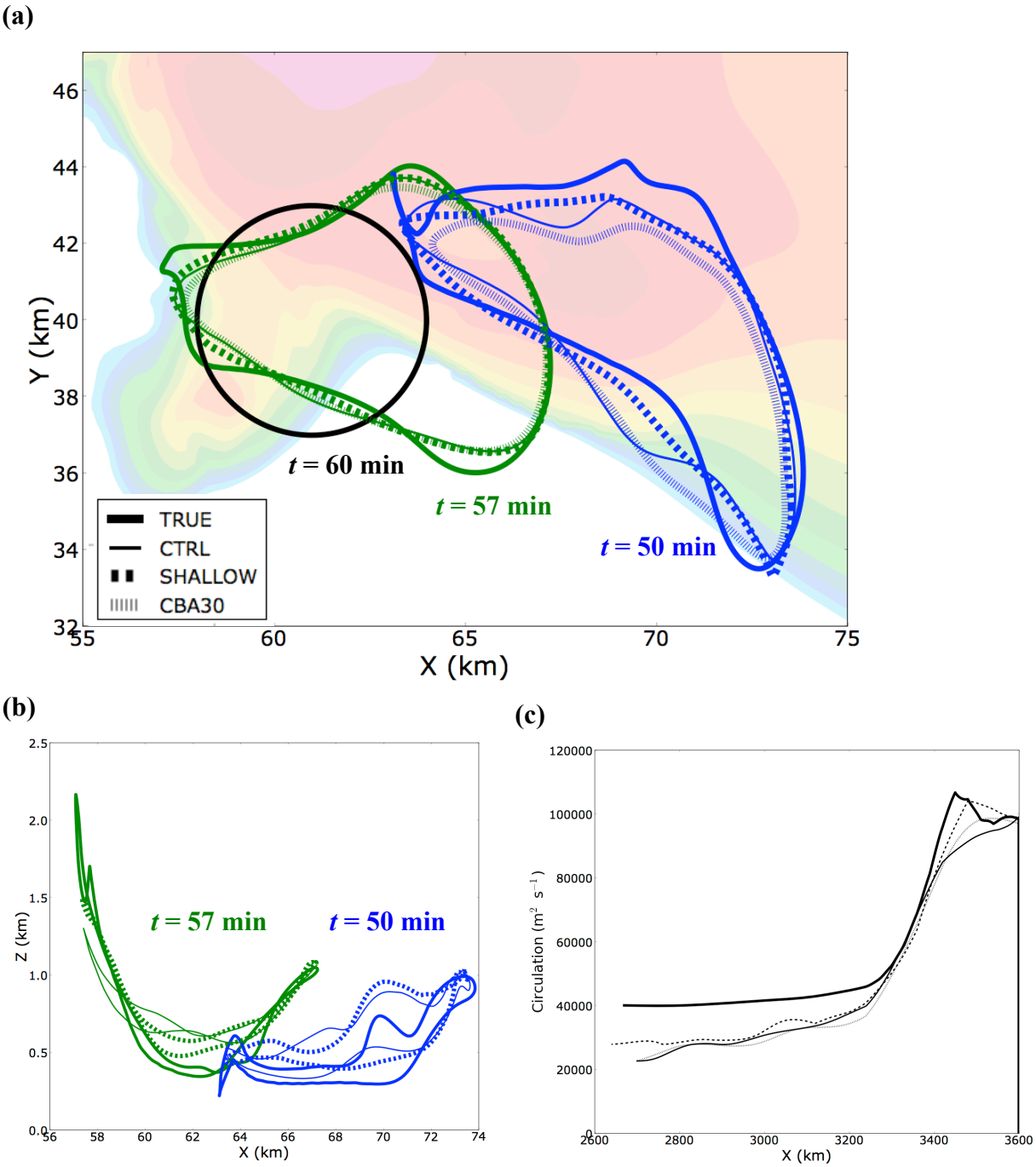

Fig. 8. (a) Horizontal projections of material circuits valid at t = 57 min (green curves) and t = 50 min (blue curves) for parcel trajectories initiated around 3-km-radius ring (black circle) at t = 60 min, z = 1.2 km. The trajectories were computed from the true (solid), CTRL (thin solid), SHALLOW (thick dashed) and CBA30 (thin dashed) wind fields. The model dBZ valid at z = 1.2 km, t = 60 min (shading) is displayed in the background. (b) Vertical (x-z) projections of the true, CTRL and SHALLOW circuits. (c) Time series of circulation computed around the circuits.